Supporting Information

Constructing Hierarchical 3D Co/N-Doped Carbon Electrocatalyst for Efficient Oxygen Reduction and Overall Water Splitting

Zengxia Pei,[a] Zijie Tang,[a] Zhuoxin Liu,[a] Yan Huang,[b] Yukun Wang,[a] Hongfei Li,[a] Qi Xue,[a] Minshen Zhu,[a] Daiming Tang,[c]* Chunyi Zhi[a, d]*

[a] Department of Materials Science and Engineering, City University of Hong Kong, 83 Tat Chee Avenue, Kowloon, Hong Kong 999077, China.
E-mail: cy.zhi@cityu.edu.hk

[b] School of Materials Science and Engineering, Harbin Institute of Technology, Shenzhen 518055, China

[c] International Center for Materials Nanoarchitectonics (MANA), National Institute for Materials Science (NIMS)
Namiki 1-1, Tsukuba, Ibaraki 305-0044 Japan
E-mail: tang.daiming@nims.go.jp.

[d] Shenzhen Research Institute
City University of Hong Kong
High-Tech Zone, Nanshan District, Shenzhen 518057, China

Experimental

Synthesis of catalysts: for the fabrication of CF-NG-Co material, 187 mg $Co(Ac)_2 \cdot 4H_2O$ was dissolved into a graphene oxide solution (1 mg mL^{-1}, 25 mL), which then subject to ultrasonic treatment followed by stirring for 20 min. Then, a piece of melamine foam (2×2×3 cm in size, *ca.* 90 mg) was immersed in the solution and was squeezed repeatedly for thorough and even adsorption of GO sheets and Co

precursor within the foam framework. After immersion for 2 hrs, the infiltrated melamine foam with adsorbed aqueous solution was carefully taken out and was dried by lyophilization technique. The thus obtained foam with GO sheets and Co^{2+} species was calcined at 800 °C for 3 hrs under Ar atmosphere with a ramp rate of 5 °C min^{-1}. In the following, the carbonized foam was immersed into 0.5 M H_2SO_4 solution at 80 °C for 10 hrs to leach out the excess and unstable Co-containing particles. Finally, the as-obtained foam was heated again at 800 °C for 1 h. Different temperatures (700/800/900 °C) were selected to check the influence of calcination temperature with the other procedures being identical. The catalyst calcined at 800 °C without the addition of Co species was marked as CF-NG. The CF sample was synthesized by mere carbonization of melamine foam.

Physicochemical Characterization. The morphology and microstructure of the samples were revealed by a Hitachi field-emission SEM and a JEOL-2001F field-emission TEM, respectively, and the accessory EELS of TEM was used to determine to composite elements. The crystal structure of the catalyst was identified by a Bruker D2 Phaser X-ray diffractometer with Cu K_α radiation (λ = 0.15418 nm) operating at 30 kV and 10 mA, respectively. Raman scattering measurements were performed with a multichannel modular triple Raman system (Renishaw Co.) with confocal microscopy at room temperature using the 633 nm laser. XPS analyses were conducted on an ESCALAB 250 photoelectron spectroscopy (Thermo Fisher Scientific) at 1.2×10^{-9} mbar using Al K_α X-ray beam (1486.6 eV). The XPS spectra

were charge corrected to the adventitious C 1s peak at 284.5 eV. TGA were carried out on a TA #SDT Q600 analyzer at 30-900 °C with an O_2 flow of 40 mL min^{-1}. The nitrogen adsorption and desorption isotherms were characterized using a Micrometrics ASAP 2020 analyzer. Pore size distribution and specific surface area were obtained via Barrett-Joyner-Halenda (BJH) and Brunauer-Emmett-Teller (BET) methods from adsorption branch of the isotherm, at a relative pressure range of P/P_0 = 0.06-0.25.

Electrochemical Measurements. All electrochemical measurements were carried out on a CHI 760D electrochemical workstation integrated with a RRDE-3A rotating ring disk electrode apparatus in a typical 3-eletrode system. A glassy carbon electrode (GCE, 3mm in diameter) loaded with different catalysts was used as working electrode, an Ag/AgCl (in 3 M KCl) electrode and a Pt mesh (or a graphitic rod for HER) served as reference and counter electrode, respectively. The recorded potential was converted to a reversible hydrogen electrode (RHE) according to the Nernst equation: $E_{RHE} = E_{Ag/AgCl} + 0.059 \times pH + 0.210$. The loading mass was 280 μg cm^{-2} for non-noble metal catalysts and 140 μg cm^{-2} for noble-metal materials (Pt/C, Alfa Acesar, 20 wt%, and IrO_2, Alfa Acesar).

ORR tests: N_2 or O_2 saturated 0.1 M KOH or 1 M KOH solution served as the electrolyte for ORR measurements. The CV curves were recorded at a scan rate of 20 mV s^{-1} and the LSV curves at 5 mV s^{-1}. The onset potential (E_{onset}) for ORR is defined as the critical potential where the reduction current density reaches 1% of the limiting

current density. All the catalysts were capacity-corrected by subtracting the background voltammograms results for the N_2-purged electrolyte from those of the O_2-purged electrolyte. Each catalyst was repeated at least 3 times for the above measurements to exclude possible incidental errors.

The RRDE tests were conducted with a Pt ring surrounded 4 mm diameter GCE (with a loading mass of 0.28 mg cm^{-2}). The Pt ring electrode was set at 1.3 V (vs. RHE) to detect the generated HO_2^- species. The value of n was also calculated through RRDE tests:

$$n = \frac{4i_d}{i_d + \frac{i_r}{N}}$$

the HO_2^- yield was calculated from equation:

$$HO_2^-\% = \frac{200i_r}{N(i_d + \frac{i_r}{N})}$$

here i_d and i_r are the disk current and ring current, respectively, and N is the current collection efficiency of the Pt ring and was determined to be 0.44.

Long term stability tests in ORR were conducted by measuring the current changes of the catalyst modified GCE at a fixed potential of 0.7 V (vs. RHE) and a rotation speed of 1600 rpm in O_2 saturated electrolyte. The cross-over tolerance tests were performed by comparing the CV curves before and after the addition of 10 vol% methanol into the electrolyte.

OER tests: the electrolyte was O_2 saturated 1 M KOH solution. The LSV curves were obtained at a scan rate of 5 mV s^{-1} and the GCE was rotated at 1600 rpm

to alleviate the accumulation of evolved oxygen bubbles on the electrode surface. The E_{onset} for OER is defined as the critical potential where the current density reaches 0.5 mA cm^{-2}. All the curves were iR corrected unless otherwise stated and in order to get a stable current, the LSV data were collected at the second sweep.

HER tests: N_2 saturated 0.5 M H_2SO_4 or 1 M KOH served as the electrolyte. A graphite rod was used as the counter electrode during the whole measurements to avoid the possible contamination of Pt species. LSV curves were carried out at 5 mV s^{-1} from 0.2 to -0.6 V (vs. RHE). All polarization curves were automatically corrected for the iR contribution from the cell. The working electrode was rotated at a speed of 1600 rpm to alleviate the accumulation of evolved hydrogen bubbles on the GCE surface. The E_{onset} for HER is defined as the critical potential where the current density reaches 0.5 mA cm^{-2}.

Zn-air battery assembly. The air electrodes for Zn-air battery use stainless steel mesh (SSM) as backing layer, with a gas diffusion layer (GDL) on the air-facing side and catalyst on the water-facing side. A carbon ink consists of carbon black and polytetrafluoroethylene (PTFE) emulsion (60 wt%) according to a mass of 3:7 was painted onto the backing layer to form the GDL, which then subject to heating at 200 °C for 30 min. The catalyst was then loaded onto the other side of the SSM by drop-casting with an identical loading mass of 1.0 mg cm^{-2} for both CF-NG-Co sample and noble metal catalyst (bare Pt/C or Pt/C-IrO_2 mixture, 0.5+0.5 mg). A polished Zn plate served as anode and the electrolyte were 6.0 M KOH for Zn-air primary

batteries and 6.0 M KOH with 0.2 M $Zn(Ac)_2$ for rechargeable Zn-air batteries. The GDL has an effective area of 1 cm^2 and allows O_2 from ambient air to reach the catalyst sites.

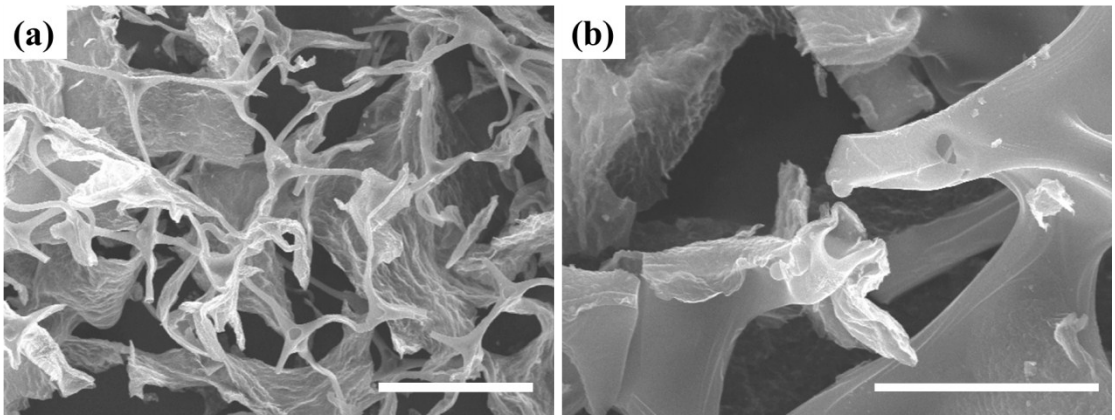

Figure S1. SEM images showing (a) the morphology of the hierarchical hybrid CF-NG-Co catalyst, and (b) the intimate grafting of graphene sheets onto the carbon foam skeleton. Scale bar: (a) 20 μm, (b) 10 μm.

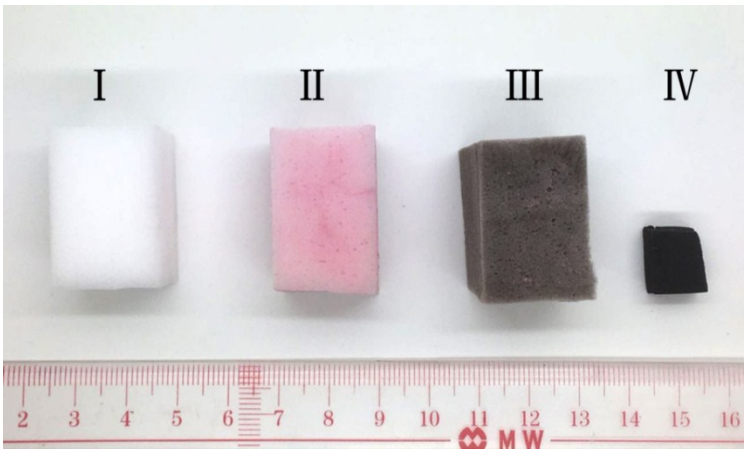

Figure S2. Digital image of the (I) pristine MF, (II) $Co(Ac)_2$ impregnated MF, (III) GO and $Co(Ac)_2$ impregnated MF, (IV) pyrolyzed CF-NG-Co sample (before acid leaching).

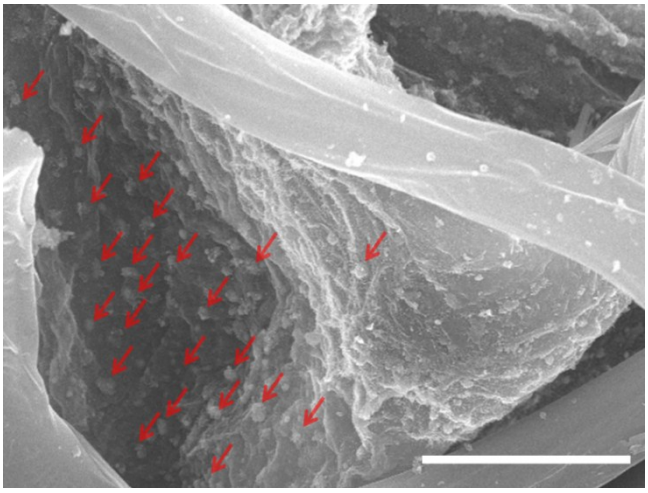

Figure S3. SEM image showing the 0D-2D-3D hierarchical structure of the hybrid CF-NG-Co catalyst. The red arrows indicate the Co particles anchoring on the N-doped graphene sheet. Scale bar, 5 μm.

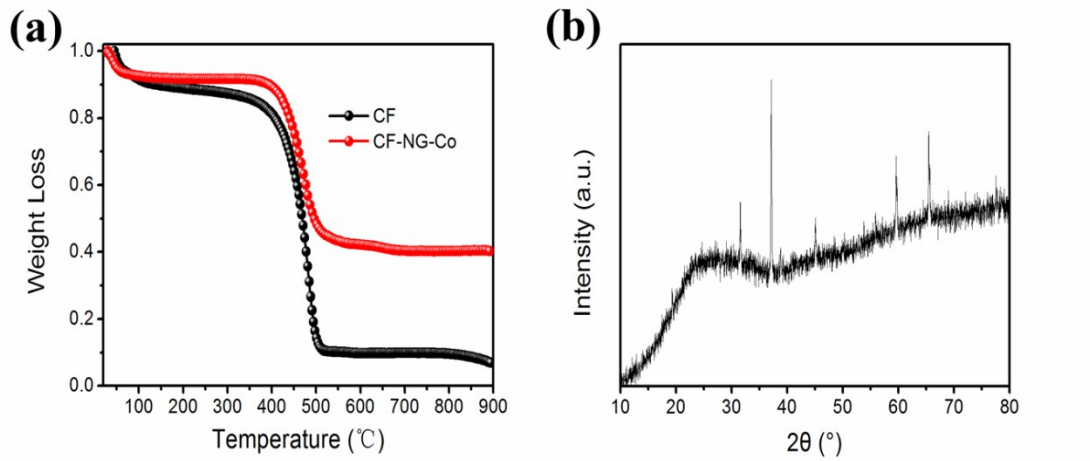

Figure S4. (a) TGA analyses of the CF-NG-Co and pure CF samples; (b) XRD patterns of the resulted black powders from the CF-NG-Co sample after combustion in O_2.

Note: the pure CF sample still left 10 wt% residuals after combustion, which is very probably from the original addictives in the melamine foam (e.g., sodium bisulfite).[1] The CF-NG-Co sample left some black powder, which was then identified to be tricobalt-tetraoxide (JCPDS No. CF-03-065-3103) by XRD patterns. According to the XRD results from the pristine CF-NG-Co samples (Figure 2b), a reliable Co content of 22.3 wt% could therefore be determined by assuming that all the cobalt species is metallic Co.

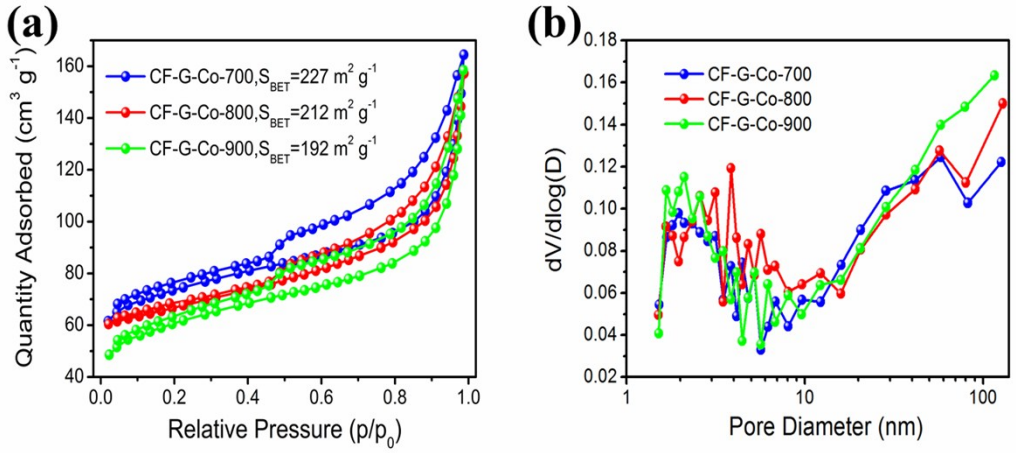

Figure S5. (a) N_2 adsorption/desorption isotherms of the CF-NG-Co series samples pyrolyzed at different temperatures; (b) Pore diameter distribution of all samples.

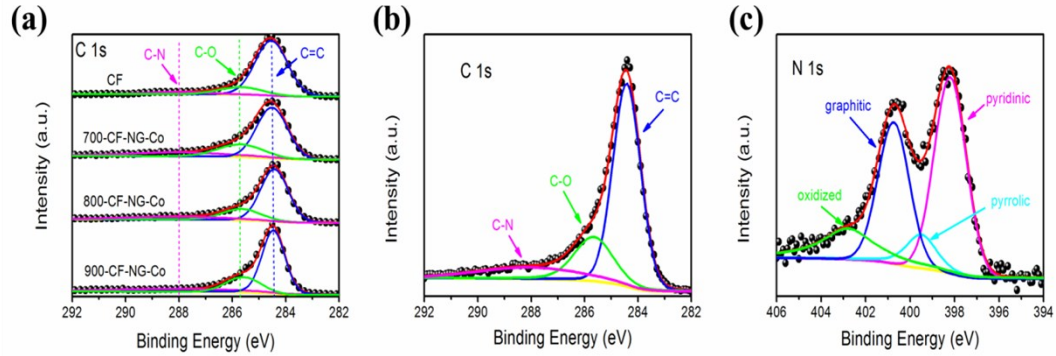

Figure S6. (a) High resolution C 1s XPS spectra of the samples. Magnified (b) C 1s and (c) N 1s core-levels of the representative 800-CF-NG-Co sample.

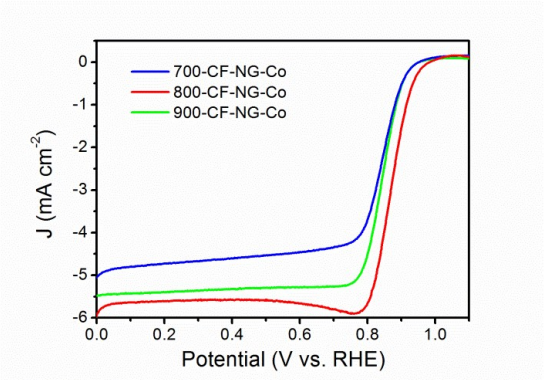

Figure S7. LSV curves for ORR in O_2 saturated 0.1 M KOH solution of the CF-NG-Co series catalysts pyrolyzed at different temperatures.

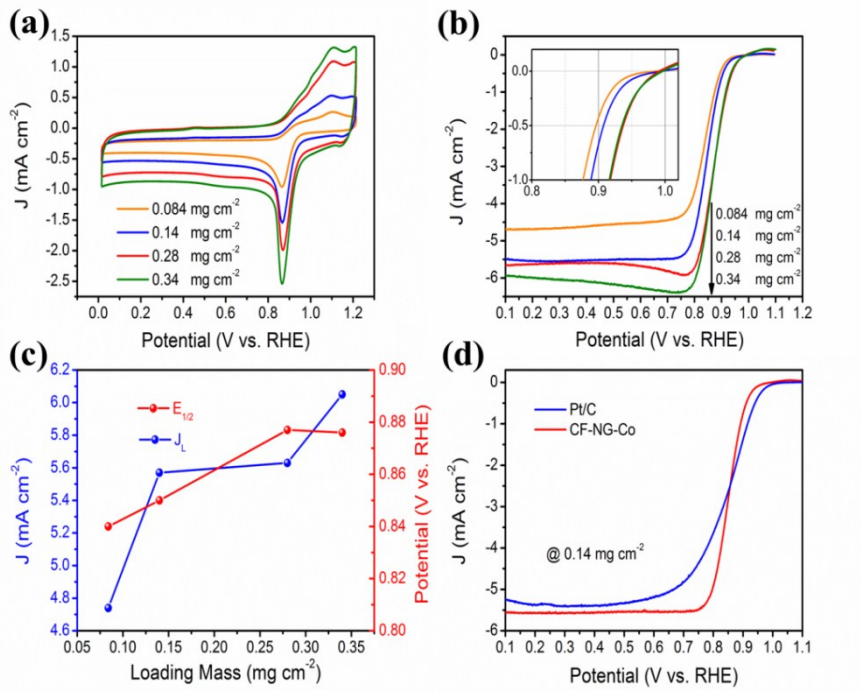

Figure S8. Influence of different loading masses on the ORR activity in O_2 saturated 0.1 M KOH: (a) CV scans (at 20 mV s^{-1}) and (b) LSV curves (at 5 mV s^{-1}, positive scan) of the the CF-NG-Co catalyst with different loading masses. (c) Comparison of the influence of loading mass on limgting current density (J_L) and half-wave potential of the CF-NG-Co catalyst. (d) LSV curves (at 5 mV s^{-1}) of the CF-NG-Co sample with the referenced Pt/C catalyst at an identical loading mass.

Note: Different laoding masses have negligible influence on the E_{onset} and the

E_{peak}, while higher loading mass will result in larger reduction current density and $E_{1/2}$. We further plot the J_L and $E_{1/2}$ against the loading mass, it is found that the J_L shows a further but compromized increase while the $E_{1/2}$ value get to a plateau when the loading mass reaches 0.28 mg cm^{-2}. Considering even larger loading mass will result in a un-negligible contribution from the static reduction current, an optimal loading mass of 0.28 mg cm^{-2} was used for the CF-NG-Co catalyst. However, note that even at a much smaller loading mass of 0.14 mg cm^{-2}, both the reduction current density and $E_{1/2}$ of the CF-NG-Co sample (5.5 mA cm^{-2} and 0.85 V, respectively) is still comparable with those from the Pt/C catalyst (5.4 mA cm^{-2}, 0.85 V) with an identical loading mass, demonstrating the excellent ORR activity of the hybrid CF-NG-Co catalyst.

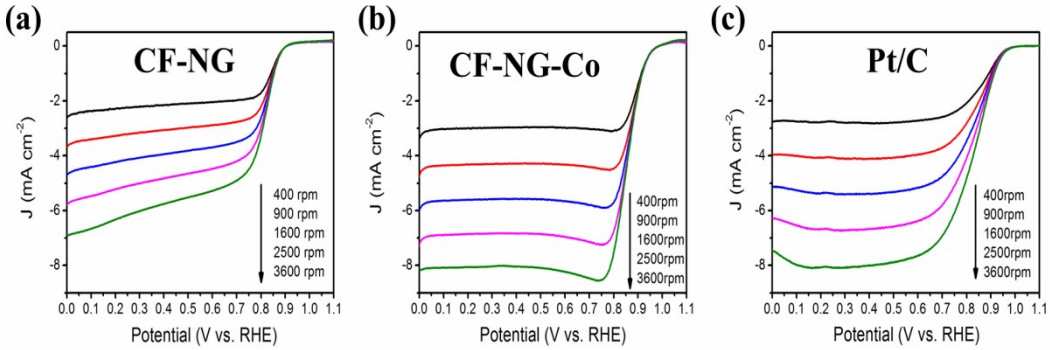

Figure S9. LSV curves of different catalysts for ORR in O_2 saturated 0.1 M KOH solution at different rotation speeds.

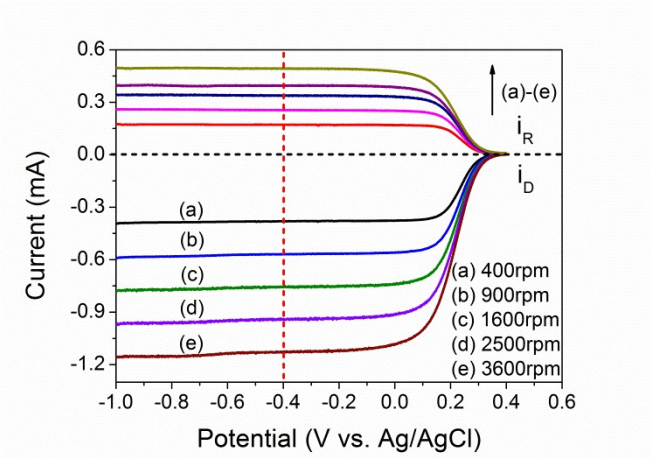

Figure S10. RRDE (Pt ring GC disk electrode) voltammograms for the reduction of $K_3[Fe(CN)_6]$ at the disk electrode in N_2 saturated aqueous KCl solution with disc scan rate of 10 mV s^{-1} at different rotation speeds.

Note: The current collection efficiency (N) of Pt ring in RRDE technique is determined by using single electron reversible couple of ferrocyanide/ferricyanide system. Specifically, a mirror-polished Pt ring GC disk electrode was immersed into N_2 saturated 0.5 M KCl solution containing 10 mM $K_3[Fe(CN)_6]$. The disk electrode was scanned between -1.0 – 0.4 V (vs. Ag/AgCl) at 10 mV s^{-1} and the ring potential was set at 0.5 V. The LSV curves were recorded at rotation speeds of 400-3600 rpm and the ratio the ring and disk limiting currents ($N = i_r/i_d$) reveals the N. In the present system, the N was determined to be 0.44 irrespective of the rotation speed.

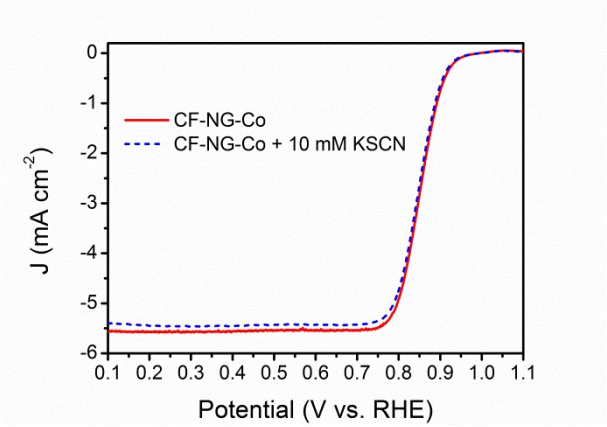

Figure S11. Steady-state LSV curves of the CF-NG-Co in O_2 saturated 0.1 M KOH before and after the addition of 10 mM KSCN; catalyst loading, 0.14 mg cm^{-2}.

Note: It is known that a series of agents (including CN^-, SCN^- et. al) can well block transitional metal species in the M-N_x motiety,[2, 3] here the KSCN salt was added into the electrolyte to review the role of Co species. Upon an addition of 10 mM KSCN and a dwelling time of 1 h, the polorization curve of the CF-NG-Co catalyst shows a discernable but slight loss in reduction current and negative shift in $E_{1/2}$, attesting that the Co-N-C motif is involved in the ORR process but only with moderate contirbution. On the other hand, the cobalt species is known for promoting the graphization of a variety of organic precursors.[4, 5] The Raman spectra (Figure 2c) show all the Co-conatinng catalysts have higher graphitization degree tan the metal-free CF-NG sample. Therefore, the Co species probably also indirectly contribute to ORR via enhancing the conductivity of the carbon scaffold and subsequently the charge transfer process.

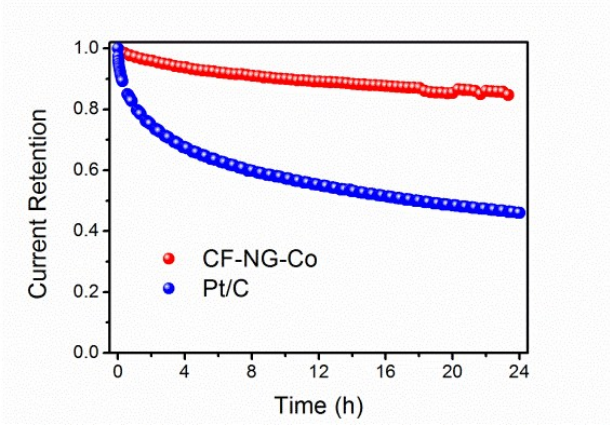

Figure S12. Chronoamperometric durability tests of the CF-NG-Co and referenced Pt/C samples at 1600 rpm and 0.7 V (vs. RHE) in O_2 saturated 0.1 M KOH.

Note: In a continuous 24 hrs amperometric i-t test at 1600 rpm and 0.7 V potential, the CF-NG-Co sample preserved 85% of its initial current, while the referenced Pt/C sample lost over 50% of its activity. The good stability of our 0D-2D-3D hybrid catalyst results probably from the intimate chemical bonding and synergetic coupling of Co/N-C complex and the robustness of the N-doped carbon skeleton, which avoids the detachment and collapse as in the Pt/C system.[6]

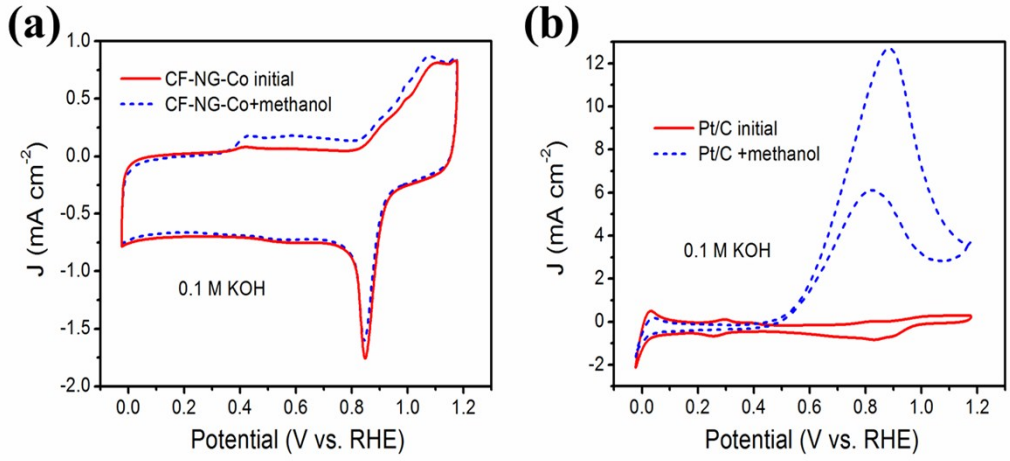

Figure S13. Cross-over tolerance tests of the representative (a) CF-NG-Co and (b) Pt/C samples before and after the addition of 10 vol% methanol into 0.1 M KOH.

Note: the hybrid CF-NG-Co catalyst shows negligible distinction with the inroduction of metahnol, suggesting the excellent selectivity towards ORR of the sample. By contrast, Pt/C modified electrode dilivers a drastic anodic current, which results from significant methanol oxidation reaction, indicating the susceptive selectivity of Pt/C catalyst.

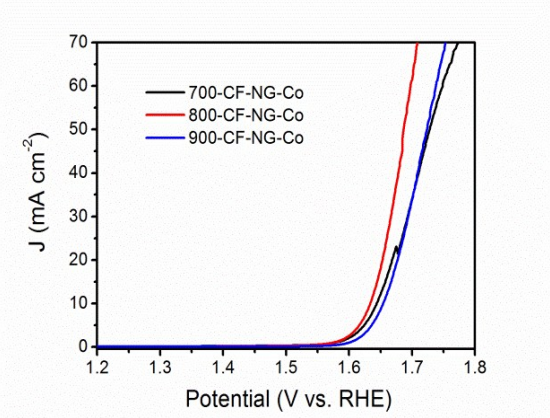

Figure S14. LSV curves of the OER performances of the CF-NG-Co series catalysts pyrolyzed at different temperatures.

Note: It is reported that the Co^{2+} species favors OH^- adsorption owing to its high electrostatic affinity, thus is beneficial for OER as compared with metallic Co.[7, 8] However, Raman spectra (Figure 2c) suggest that the 700 °C pryolyzed sample features the lowest I_D/I_G ratio, suggesting its poor conductivity. Therefore, the 700-CF-NG-Co sample, though with the highest Co^{2+} content (XPS results in Figure 2f), still exhibits unsatisfactory OER activity. The 900 °C pyrolyzed catalyst, on the contrary, suffers from limited amount of Co^{2+} active sites despite with better graphitization degree. Though further investigations are needed to in-depth reveal the activity performance difference resulting from the pryolysis temperature, it is reasonably deduce that the electrocatalytic activity are closly governed by the

concentration of active species and the conductivity. The 800-CF-NG-Co catalyst poessesses a desirable amount of Co^{2+} species in conjuction with a preferable conductivity, thus affords the best OER as observed here. On the other hand, the N/C atomic ratio by XPS analyses was determined to be 10.7%, 6.8% and 3.8% for the 700 °C, 800 °C and 900 °C pyrolyzed samples, respectively. The suitable N heteroatom concentration may also contribute to the OER activity of the CF-NG-Co catalyst, as proven in Figure 4a.

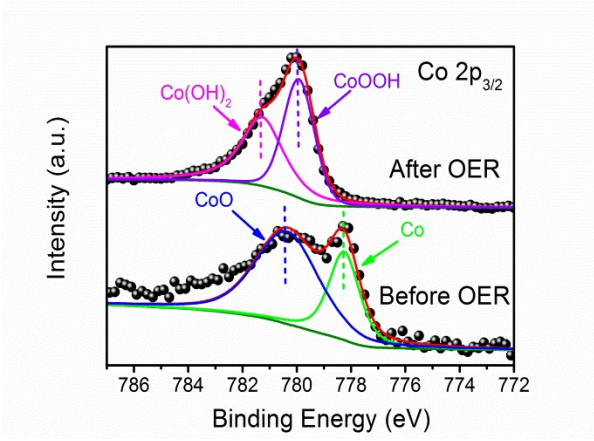

Figure S15. Co $2p_{3/2}$ XPS fine spectra reviewing the change of the oxidation states of Co within the CF-NG-Co sample before and after OER tests.

Note: The harsh oxidative aqueous environment during OER could thermodynamically oxidize the metallic Co and CoO species. In this sence, after OER tests in O_2 saturated 1 M KOH, XPS analysis was further conducted to check the oxidation states of the Co element. As shown in Figure S15, the characteristic fine Co $2p_{3/2}$ core level exhibites obvious distinctions compared with that before OER tests. After OER, the peak centered at 781.3 eV can be assigned to Co atoms in the $Co(OH)_2$ species while the other one located at 779.9 eV is attributed to that in OER-active CoOOH phase,[9,10] distinguishing with the pristine metallic Co (778.3 eV) and CoO (780.4 eV) before OER. It is reasonable that Co atoms in the as-synthesied sample existed as low oxidation status owing to the reduction during the thermal pyrolysis (Figure 2f), which were then hydroxylated and oxidized to higher oxidation

states in the aqueous OER environment. This oxidation process also accounts for the observed oxidation peaks at high potential (~ 1.1-1.2 V_{RHE}) in the CV scans during ORR (Figure 3a, S8a). Therefore, it is believed that the Co species in the CF-NG-Co sample underwent an *in-situ* transformation process to initiate the OER, similar to some recent other studies.[9, 11, 12]

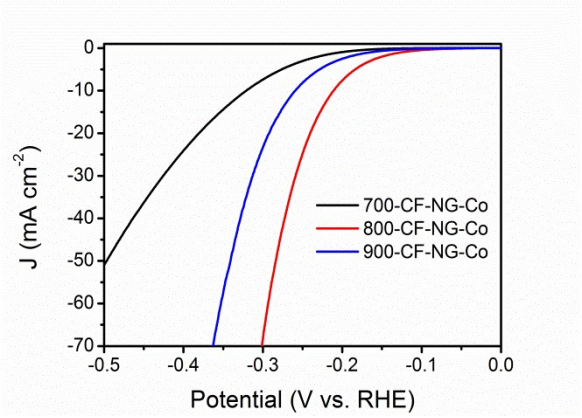

Figure S16. LSV curves of the HER performance in 1 M KOH of the CF-NG-Co series catalysts pyrolyzed at different temperatures.

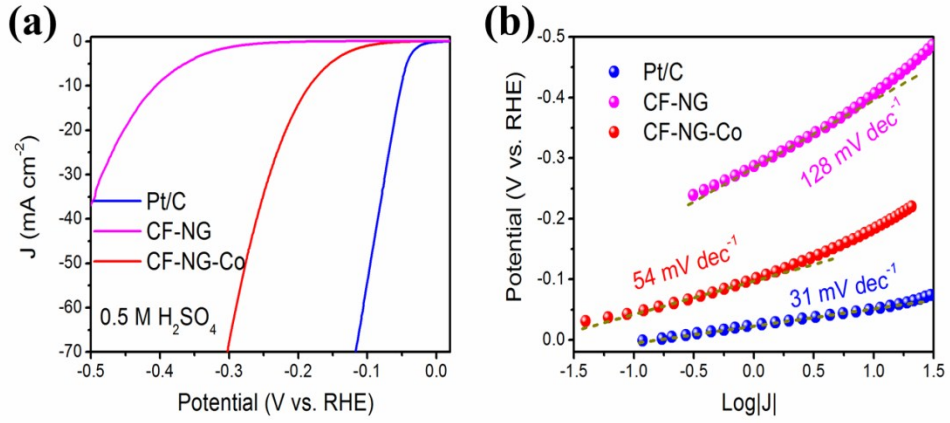

Figure S17. Electrochemical catalytic performance toward HER in 0.5 M H_2SO_4 solution: (a) polarization curves of different catalysts on RDE with a scan rate of 5 mV s^{-1} at 1600 rpm; (b) corresponding Tafel plots of varied catalysts derived from curves in (a).

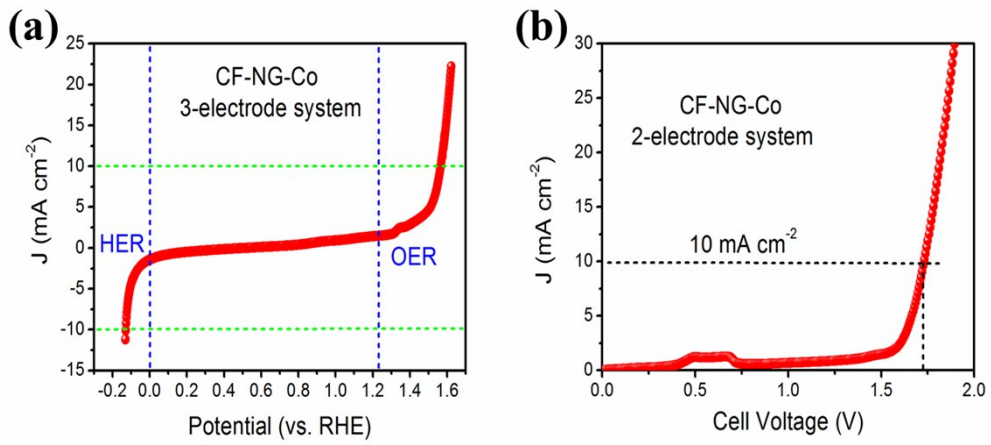

Figure S18. Overall water splitting perforamnce recorded in 1 M KOH using the CF-NG-Co/Ni foam as work electrode and counter electrode in a typical 3-electrode system (a) or anode and cathode in a 2-electrode (b) system. The loading mass of the catalyst was 200 mg cm^{-2} for all the electrodes. All the data are not iR-corrected.

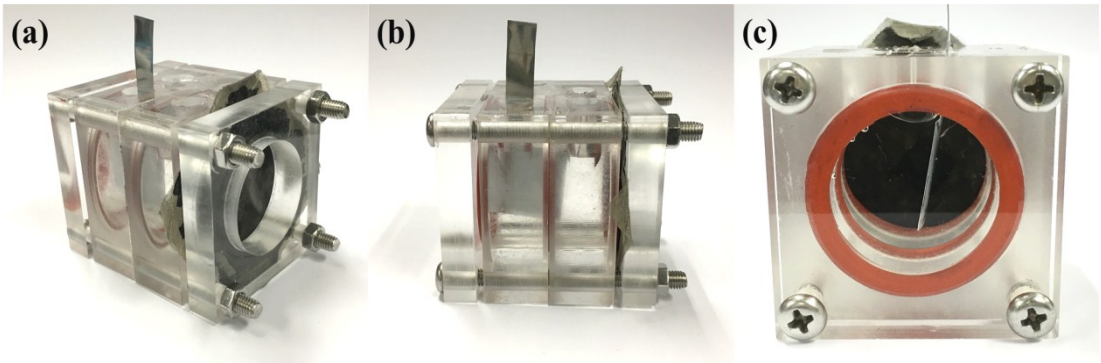

Figure S19. Side-view (a) & (b) and front-view (c) of the static Zn-air battery device. The catalyst was casted onto the gas diffusion layer with a geometric area of 1×1 cm.

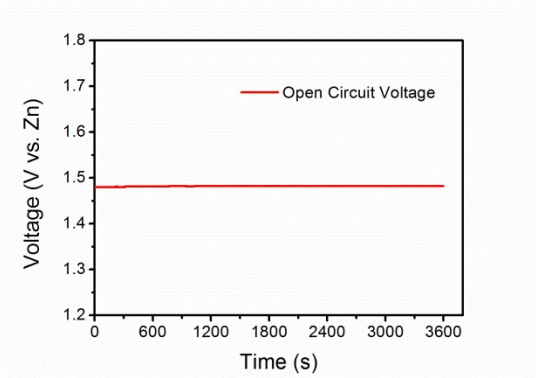

Figure S20. Open circiut voltage(vs. Zn) of the Zn-air battery based on the CF-NG-Co catalyst recorded in 6 M KOH solution within 3600s.

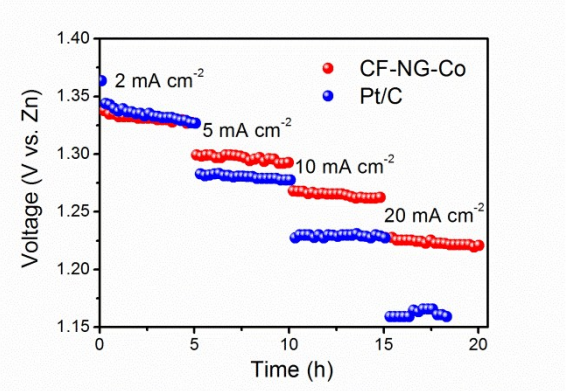

Figure S21. Galvanostatic discharge curves of the primary Zn-air batteries based on CF-NG-Co and Pt/C samples at different current densities, which were normalized to the area of the air cathode.

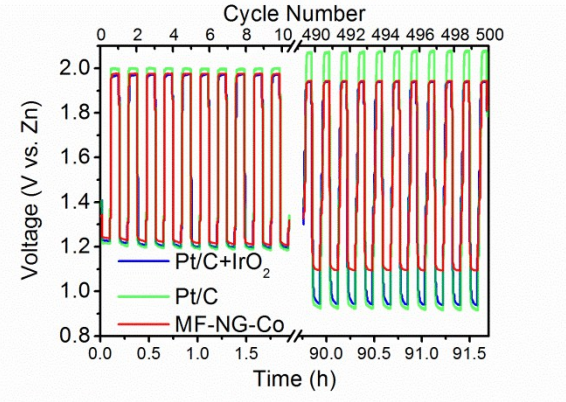

Figure S22. Magnified first and last 10 cycles of rechargeability test of the Zn-air battery based on different samples at 10 mA cm^{-2}.

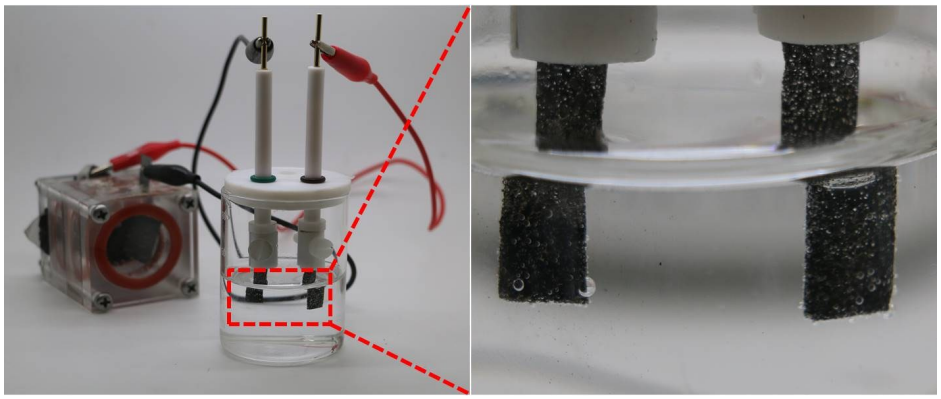

Figure S23. (a) The self-powered water-splitting system driven by Zn-air battery (ORR) all based on the CF-NG-Co catalyst. The catalyst was loaded onto Ni foam for OER and HER with a loading mass of 2 mg cm^{-2}, and the electrolyte was 1 M KOH. (b) The magnified electrode surface showing the evolved bubbles from water splitting reaction after a duration time of 1 h.

Table S1 Comparison study of some advanced ORR catalysts in 0.1 M KOH electrolyte

Catalyst	Loading Mass (mg cm^{-2})	Onset Potential (V vs. RHE)	Half-wave Potential (V vs. RHE)	Limiting-Current Density @1600 rpm (mA cm^{-2})	Reference
N-doped carbon nanotube arrays	-	0.97	0.84	5.6	Science **2009**, 323, 760
B, N-graphene	0.28	0.86	0.68	5.2	Angew. Chem. Int. Ed. **2013**, 52, 3110
Porous Fe-N_x-C	0.2	1.01	0.86	5.1	ACS Catal. **2014**, 4, 1793
N-doped meso/micro porous carbon	0.1 (0.5)	0.92 (0.92)	0.85 (0.87)	5.8 (5.8)	Nature Commun. **2014**, 5, 4973
Fe_3C/C	0.6	1.05	0.83	5.3	Angew. Chem. Int. Ed. **2014**, 53, 3675
N, P-doped mesoporous carbon	0.15	0.94	0.85	4.3	Nature Nanotech. **2015**, 10, 444
Fe_3C@NG	0.4	1.03	0.86	5.5	Adv. Mater. **2015**, 27, 2521
N/Co-doped PCP//NRGO	0.714	0.97	0.86	7.5	Adv. Funct.Mater. **2015**, 25, 872.
Fe-N-C capsules	0.1	0.94	0.83	4.9	ACS Nano **2016**, 10, 5922
Fe_2O_3-N-doepd Graphene	0.1	0.91	0.85	5.9	ACS Catal. **2016**, 6, 3558
N-doped porous carbon fiber	0.1	0.97	0.82	4.7	Adv. Mater. **2016**, 28, 3000
N, S-doped Graphene sheets	0.2	0.92	0.77	4.4	Nano Energy **2016**, 19, 373
NiFe/N-doped Graphene	0.4	1.03	0.86	5.9	ACS Catal. **2016**, 6, 6335
Co-N-CNT Frameworks	0.2	0.97	0.87	5.2	Nature Energy, **2016**, 1: 15006
Co_3O_4-N-doped porous carbon	0.2	0.97	0.84	5.8	Angew. Chem. Int. Ed. **2016**, 55, 4977
N, S-doped porous carbon	0.14 (0.42)	0.99 (0.99)	0.85 (0.88)	5.8 (6.4)	Energy Environ. Sci. **2017**, 10, 742

CF-NG-Co	0.28 (0.14)	0.97 (0.97)	0.88 (0.85)	5.6 (5.5)	This work

Table S2 Comparison study of some recently reported bi-functional ORR/OER catalysts in alkaline electrolyte

Catalyst	Loading Mass (mg cm^{-2})	OER Onset Potential (V vs. RHE)	OER $E_{J=10}$ (V vs. RHE)	OER Tafel Slope (mV dec^{-1})	ΔE ($E_{j=10}$ - $E_{1/2}$) (V)	Electrolyte	Reference
MnO_x Film	-	1.30	1.77	-	1.04	0.1 M KOH	J. Am. Chem. Soc. **2010**, 132, 13612
Co_3O_4/N-doped graphene	1.0	1.40	1.54	67	0.71	1 M KOH	Nat. Mater. **2011**, 10, 780
H-Pt/$CaMnO_3$	0.085	1.50	1.80	-	1.01	0.1 M KOH	Adv. Mater. **2014**, 26, 2047
Mn_xO_y/N-doped carbon	0.21	1.55	1.68	-	0.87	0.1 M KOH	Angew. Chem. Int. Ed. **2014**, 53, 8508
CoO/N-doped graphene	0.7	1.30	1.57	71	0.76	1 M KOH	Energy Environ. Sci. **2014**, 7, 609
Fe@N-C	0.31	*ca.* 1.52	1.71	-	0.88	0.1 M KOH	Nano Energy **2015**, 13, 387
N/Co-doped PCP//NRGO	0.357	-	1.66	292	0.8	0.1 M KOH	Adv. Funct.Mater. **2015**, 25, 872.
N-doped porous carbon fiber	0.1	1.43	1.84	274	1.02	0.1 M KOH	Adv. Mater. **2016**, 28, 3000
N-doped graphene	0.3	1.51	1.59	47	0.75	1 M KOH	Sci. Adv. **2016**, 2:e1501122
N, S-doped Graphene sheets	0.2	1.59	1.65	53	0.88	0.1 M KOH	Nano Energy **2016**, 19, 373
NiFe/N-doped Graphene	0.4	1.46	1.55	61	0.7	0.1 M KOH	ACS Catal. **2016**, 6, 6335
Co-N-CNT Frameworks	0.2	-	1.60	93	0.73	0.1 M KOH	Nature Energy, **2016**, 1: 15006
Co_3O_4-N-doped porous carbon	0.2	-	1.68	-	0.84	0.1 M KOH	Angew. Chem. Int. Ed. **2016**, 55, 4977
NiCo/PFC aerogels	0.13	-	1.63	106	0.86	0.1 M KOH	Nano Lett. **2016**, 16, 6516
N, S-doped graphitic sheets	0.2	1.49	1.60	71	0.77	0.1 M KOH	Adv. Mater. **2017**, 29, 1604942
FeCo-N-doped CNT	0.2	-	1.73	100	0.81	0.1 M KOH	Adv. Energy Mater. **2017**, 1602420

CF-NG-Co	0.28	1.55	1.63	60	0.75	1 M KOH	This Work

Table S3 Comparison study of some advanced HER catalysts in different electrolytes

Catalyst	Loading Mass (mg cm^{-2})	Onset Potential (V vs. RHE)	HER $E_{J=10}$ (V vs. RHE)	HER Tafel Slope (mV dec^{-1})	Electrolyte	Reference
MoO_3-MoS_2 Nanowires	0.06	-(150-200)	~ -250	50-60	0.5 M H_2SO_4	Nano Lett. **2011**, 11, 4168.
MoS_2 Nanosheets	0.285	-120	~ -180	50	0.5 M H_2SO_4	Adv. Mater. **2013**, 25, 5807.
CoS_2 NW CoS_2 MW	-	-75 -75	-145 -158	52 58	0.5 M H_2SO_4	J. Am. Chem.Soc. **2014**, 136,10053
Co-N-CNT	0.28	-50 -	-260 -370	80 -	0.5 M H_2SO_4 (1 M KOH)	Angew. Chem. **2014**, 126, 4461
C_3N_4@NG	~0.1	-	-240	51	0.5 M H_2SO_4	Nature Comm. **2014**, 5, 3783.
N,S-doped Graphene 500C	-	-130	-276	81	0.5 M H_2SO_4	Angew. Chem. Int. Ed. **2015**, 54, 2131.
Co_9S_8@C	0.3	-	-240 -250	-	0.5 M H_2SO_4 (1 M KOH)	ACS Appl. Mater. Interfaces **2015**, 7, 980
N/Co-doped PCP//NRGO	0.357	-58	-229	126	0.5 M H_2SO_4	Adv. Funct.Mater. **2015**, 25, 872.
Porous CoN_x/C	2	-20	-133	57	0.5 M H_2SO_4	Nat. Comm. **2015,** 6, 7992
Co@NG	1.08	-50 -70	-183 -220	100 (112)	0.5 M H_2SO_4 (1 M KOH)	Adv. Funct.Mater. **2016**, 26, 4397
Mo_2C/N-doped carbon microflowers	0.28	-40 -	-144 -100	55 65	0.5 M H_2SO_4 (1 M KOH)	ACS Nano, **2016**, 10, 11337
Hollow $NiMo_3S_4$	0.3	-59	-257	98	0.1 M KOH	Angew.Chem. **2016**, 128,15466
N, S-doped graphitic sheets	0.2	-230	-310	112	0.1 M KOH	Adv. Mater. **2017**, 29, 1604942
CF-NG-Co	0.28	-81 (-104)	-183 (-212)	54 (75)	0.5 M H_2SO_4 1 M KOH	This work

Table S4 Comparison study of rechargeable Zn-air batteries based on different reversible oxygen catalyst

Catalyst	Loading Mass (mg cm^{-2})	Power Density (mW cm^{-2})	Energy Density based on Zn (Wh kg^{-1}_{Zn})	Cycling Conditions (mA cm^{-2})	Round-trip Efficiency	Stability	Reference
Co_3O_4 nanowires on stainless steel	-	40	-	17.6	45%	10 min/cycle for 100 cycles; voltage gap increased ~0.1 V	Adv. Energy Mater. **2014**, 4, 1301389
MnO_x on stainless steel	0.3	27	-	20	45%	-	Energy Environ. Sci. **2014**, 7, 2017
N, P-doped mesoporous carbon	0.5	55	835@5 mA cm^{-2} 695@25 mA cm^{-2}	2	59%	10 min/cycle for 180 cycles; voltage gap increased ~0.7 V	Nature Nanotech. **2015**, 10, 444
B, N-doped porous carbon	3	14.6	-	20	46%	10 min/cycle for 66 cycles; voltage gap increased ~0.02 V	Adv. Mater. **2015**, 27, 3789
P-doped C_3N_4 on carbon-fiber paper	-	-	-	20	42.7%	10 min/cycle for 50 cycles; negligible change	Angew. Chem. Int. Ed. **2015**, 54, 4646
Fe@N-C	2.2	220	-	10	64%	10 min/cycle for 100 cycles; voltage gap increased ~0.16 V	Nano Energy **2015**, 13, 387
Co_3O_4–NCNT on stainless steel	-	160.7	848@5 mA cm^{-2} 803@50 mA cm^{-2}	25	61%	20 min/cycle for 1500 cycles; voltage gap increased ~0.16 V	*Adv. Mater.* **2016**, 28, 6421
N-doped graphene	0.5	65	-	2	*ca.* 60%	60 min/cycle for 150 cycles; voltage gap increased ~0.2 V	Sci. Adv. **2016**, 2:e1501122
N-doped porous carbon fiber	2	185	838@5 mA cm^{-2} 776@10 mA cm^{-2}	10	62%	10 min/cycle for 500 cycles; voltage gap increased ~0.13 V	Adv. Mater. **2016**, 28, 3000
Co_3O_4-N-doped porous carbon	0.9	-	-	5	-	20 min/cycle for 250 cycles; negligible change	Angew. Chem. Int. Ed. **2016**, 55, 4977
NiFe/N-doped Graphene	1	*ca.* 80	732@10 mA cm^{-2}	10	76.7%	10 min/cycle for 205 cycles; voltage gap increased ~0.29 V	ACS Catal. **2016**, 6, 6335
N, S-doped porous carbon	2	151	-	10	61%	11 min/cycle for 300 cycles; voltage gap increased ~0.085 V	Energy Environ. Sci. **2017**, 10, 742
FeCo-N-doped CNT	2	89.3	653@100 mA cm^{-2}	120	32.3%	10 min/cycle for 240 cycles; voltage gap increased ~0.03 V	Adv. Energy Mater. **2017**, 1602420

CF-NG-Co	1	160	929@10 mA cm^{-2}	10	63%	11 min/cycle for 500 cycles; voltage gap increased ~0.12 V	This work

References

S1. L. Zhu, C. Fu Tan, M. Gao, G. W. Ho, *Adv. Mater*. 2015, **27**, 7713-7719.

S2. R. A. Rincn, J. Masa, S. Mehrpour, F. Tietz, W. Schuhmann, *Chem. Commun*. 2014, **50**, 14760-14762.

S3. J. Liu, X. Sun, P. Song, Y. Zhang, W. Xing, W. Xu, *Adv. Mater*. 2013, **25**, 6879-6883.

S4. K. H. Lim, H. Kim, *Appl. Catal. B: Environ.* 2014, **158,** 355-360.

S5. N. S. Kim, Y. T. Lee, J. Park, J. B. Han, Y. S. Choi, S. Y. Choi, J. Choo, G. H. Lee, *J. Phys. Chem. B* 2003, 107, 9249-9255.

S6. Z. Pei, H. Li, Y. Huang, Q. Xue, Y. Huang, M. Zhu, Z. Wang, C. Zhi, *Energy Environ. Sci.* 2017, **10**, 742-749.

S7. X. Liu, W. Liu, M. Ko, M. Park, M. G. Kim, P. Oh, S. Chae, S. Park, A. Casimir, G. Wu, *Adv. Funct. Mater.* 2015, **25**, 5799-5808.

S8. H. Jin, J. Wang, D. Su, Z. Wei, Z. Pang, Y. Wang, *J. Am. Chem. Soc.* 2015, **137**, 2688-2694.

S9. L. Pei, Z. Xu, Z. Shi, H. Zhu, S. Yan and Z. Zou, *J. Mater. Chem. A*, 2017, **5**, 20439-20447.

S10. J. Chastain, R. C. King and J. Moulder, *Handbook of X-ray photoelectron spectroscopy: a reference book of standard spectra for identification and*

interpretation of XPS data, Physical Electronics Division, Perkin-Elmer Corporation Eden Prairie, Minnesota, 1992.

S11. H. Jin, J. Wang, D. Su, Z. Wei, Z. Pang and Y. Wang, *J. Am. Chem. Soc*, 2015, **137**, 2688-2694.

S12. Z. Dai, H. Geng, J. Wang, Y. Luo, B. Li, Y. Zong, J. Yang, Y. Guo, Y. Zheng and X. Wang, *ACS nano*, 2017, DOI: 10.1021/acsnano.7b05050.